HiSST: International Conference on
High-Speed Vehicle Science Technology

26–29 November 2018, Moscow, Russia

A Transpiration Cooled Wedge with adapted Permeability

Christian Dittert[1], Hannah Böhrk[2] and Stefan Löhle[3]

Abstract

A re-entry body with sharp leading edges has advantages in aerodynamic performance, but the expected thermal loads exceed the limits of known materials. Active cooling methods are one possibility reducing surface temperatures to below the operating temperature of the used materials. The cooling effect of transpiration cooling is achieved through two basic mechanisms. When flowing through a porous, permeable material, the heat load is convectively transferred from the material to the fluid. As soon as the fluid flows out on the outside, it additionally forms a cooling film on the outside of the material, which reduces the heat flow acting on the material. However, pressure and temperature gradients along the leading edge geometry are redirecting the cooling flow in the direction of less loaded areas.
This paper presents that transpiration cooling can be effectively used for cooling sharp leading edges as demonstrated during a plasma wind tunnel campaign at the Institute of Space Systems. During this campaign a wedge geometry comparable to a re-entry leading edge with adaptable permeability, was successfully tested at re-entry heat flux conditions with different cooling mass flows rates. In addition to the plasma wind tunnel tests, the structural design and the manufacturing of the wedge are presented as well. Reference measurements without cooling indicated surface temperatures up to 1600K near the stagnation point. First results with cooling showed that even for small cooling mass flows (0.85g/s) a cooling efficiency of over 50% can be achieved for the tip area. Towards the rear region the cooling efficiency is even increasing up to 70%. Additional measurements with different angles of attack indicate that oblique shocks have an effect on the outflow distribution. Finally, the wedge geometry is assessed with regards to its applicability as leading edge on the basis of the material temperatures determined during cooling.

Keywords: *transpiration-cooling, heat transfer, re-entry, sharp leading edge, high enthalpy flow*

Nomenclature

Latin
T – Temperature
p – Pressure
k – Permeability
v – Velocity
c_p – Heat capacity
e' – Porosity
Greek
ρ – Density
μ – Viscosity
λ – Thermal conductivity
θ – Cooling efficiency
Subscripts
amb – ambient
res – reservoir
D – Darcy
F – Forchheimer
x,y,z – Directions

[1]*Research engineer, DLR, Pfaffenwaldring 38-40 70569 Stuttgart, Christian.Dittert@dlr.de*
[2]*Research scientist, DLR, Pfaffenwaldring 38-40 70569 Stuttgart, Hannah.Boehrk@dlr.de*
[3]*Research scientist,Group Leader, High Enthalpy Flow Diagnostics, IRS, University of Stuttgart*

1. Introduction

Sharp leading edges offer advantages in aerodynamic performance as they are known to induce minimum drag, require low thrust during ascent and achieve high cross-range during re-entry, leading to larger re-entry windows [18]. However, they are subject to severe aerothermodynamic loads [16]. The shock formed ahead of the vehicle upon re-entry into the atmosphere stands ahead of blunt shapes but may be attached to pointed shapes. Blunt bodies are therefore commonly used in order to increase the shock distance from the thermal protection system (TPS) and reduce the thermal load. However, the recent progress in material development and the improvement of layout and design methods allows for a reconsideration of sharp leading edge concepts for hypersonic flight [8].

Depending on the flight condition, even for high temperature materials, such as ceramic matrix composites, temperatures of sharp leading edges can exceed the tolerable material temperature. In order to face high heat loads, an active cooling concept like transpiration cooling can be a promising approach [7]. Transpiration cooling protects the material by two thermodynamic mechanisms. Firstly by flowing through the open pores, where the heat loaded material is convection-cooled and secondly the fluid forms a cooling film layer on the surface which protects the material from incoming heat from the surrounding gas [19].

Until now, porous Carbon/Carbon (C/C) has been the material of choice to design a transpiration cooled system, due to its natural permeability [6][10]. It was used in both ground testing and in the first transpiration-cooled hypersonic flight experiment onboard the re-entry experiment SHEFEX II [2]. Compared to C/C, C/C-SiC offers enhanced oxidation resistance and improved mechanical behavior in the highly thermo-mechanically loaded regime of e.g. hypersonic flight in the earth atmosphere [11][23]. This is particularly important in high temperature atmospheric environments containing atomic and molecular oxygen. A permeable C/C-SiC material, so called OCTRA (Optimized Ceramic for Transpiration) has therefore been developed for transpiration cooling of structural components such as the leading edge wedge [4]. OCTRA offers an additional advantage in the distribution of cooling mass flows, as permeability can be adapted over a wide range with this material. This makes it possible to compensate the redirection of the cooling mass flow caused by pressure and temperature gradients. Therefore, a gradation of the permeability along the wedge is chosen for the investigated wedge to ensure cooling up to the tip.

For the investigation of the cooling performance of the wedge with different permeabilities along the wedge length, wind tunnel tests with the High Enthalpy Flow Diagnostics Group(HEFDiG) at the Institute of Space Systems of the University of Stuttgart were conducted. The diagnostic equipment of the group allows to quantify the transpiration cooling under flight relevant loads. The good cooperation between the High Temperature Management for Hypersonic Flight (HiT) group at DLR and HEFDiG provides an ideal combination for the assessment of the wedge.

In this work, we will introduce transpiration-cooling, followed by describing the design and the manufacturing of a multi-layered C/C-SiC based wedge with adaptable permeability. Then the experiments conducted in a high enthalpy air flow at HEFDiG/IRS are presented, as well as the results and the efficiency achieved by transpiration cooling.

2. Transpiration Cooling

Transpiration cooling is an active cooling method using two cooling mechanisms in order to reduce material temperatures. The materials used are porous CMC materials, as transpiration cooling requires permeable materials. In order to achieve cooling, a fluid flows through the porous material and absorbs heat from the material as it flows through. The absorbed heat depends strongly on the internal structure of the material such as pore diameter and tortuosity [9][21]. The second cooling effect is comparable to film cooling, as the cooling fluid forms a protective coolant layer across the material surface and thus reduces the effective heat flux into the material [14].

The challenges of transpiration cooling of a wedge geometry exposed to a flow, as shown in Fig. 1, are both pressure and temperature gradients along the surface and within the structure, as shown schematically in Fig. 1. The Darcy Forchheimer equation describes how the cooling fluid flows through the porous material and is distributed along the material.

$$-\nabla p = \frac{\mu}{k_D} v + \frac{\rho}{k_F} v^2 \tag{1}$$

In this equation, ∇p is the pressure gradient in x, y and z, which is dependent on the flow velocity v, the viscosity μ and density ρ of the fluid and on the Darcy k_D and Forchheimer coefficient k_F, which are material parameters. Viscosity in particular has a significant influence on the flow distribution within the material. Hence, the viscosity is directly related to the fluid temperature and therefore, indirectly with the material temperature. This means, if fluid temperature rises and therefore viscosity increases as a result, the pressure drop increases over the material while the mass flow remains constant. In the application, however, the pressure remains constant so the mass flow distribution shifts to a colder area.

Taking into account the Darcy- Forchheimer equation (1) and the knowledge that different pressures and temperatures occur along the wedge, the cooling fluid will not be distributed homogeneously over the wedge. As indicated in Fig. 1, less cooling fluid would be exhausted along the bottom side than along the top depending on the angle between velocity vector an wedge. This is due to the stronger shock compared to the top side, which leads to a higher counter pressure and subsequently lower pressure loss at the bottom, which results in lower outlet velocities.

In addition, the viscosity at the bottom side rises much more rapidly due to the higher temperature and thus additionally blocks the cooling fluid from flowing through. In summary, in non-homogeneous external conditions, the cooling fluid flows to the cold side and along the highest pressure drop. In order to counteract these effects, the presented wedge is equipped with functionally graded permeability k_D and k_F and the wall thicknesses are locally adapted, as presented in the Sec. 4.

3. Plasma Wind Tunnel PWK4

For the present investigation the plasma wind tunnel PWK4 shown in Fig. 2 was used [1]. It provides high enthalpy, supersonic air plasma flows relevant for the investigation of Earth entries from low earth orbits at altitudes between 50 km and 30 km.
The plasma wind tunnel PWK4 is equipped with a thermal arc-jet generator RB3, which is attached to the movable front lid of the vacuum chamber (diameter: 2 m, length: 6 m). Vacuum is realized with a centralized common vacuum pumping system. A major refurbishment of this system in 2014 resulted in lower end pressure in the chamber and additional advantage of the new system is the improved ambient pressure control [17]. The vacuum chamber walls are water-cooled and a high pressure water cooling circuit provides high cooling rates for the copper cooling shields and the sample holder inside the vacuum chamber. A movable platform allows fast and programmable positioning of probes and samples

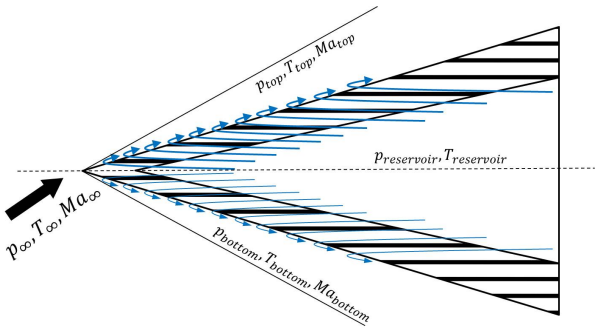

Fig 1. Transpiration cooling through a wedge geometry

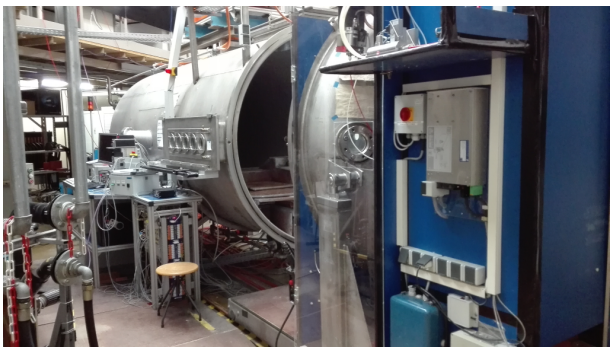

Fig 2. Plasma wind tunnel PWK4 at IRS.

Table 1. PWK4 flow condition

voltage	93 V
current	600 A
N_2 mass flow rate	5.0 g/s
O_2 mass flow rate	1.52 g/s
total pressure	1250 Pa
measurement position x	90 mm
reference heat flux	MW/m^2
flat faced cyl. dia. 50mm	0.85
sphere dia. 50mm	1

on a sample holder with respect to the plasma plume axis (direction x) and the nozzle exit plane. Depending on the back pressure in the chamber, the position in the flow with respect to the nozzle exit plane, the gas mass flow and input power on the generator, a flow condition is defined. The power supply system at IRS is a 6 MW DC power converter based on six current-regulated thyristor rectifiers. The flow condition used for the present investigations is given in Tab. 1.

4. Material Choice and Wedge Design

In the design of the wedge, particular attention was paid to the outflow distribution across the surface, to ensure transpiration cooling up to the tip. Moreover, although only used in ground testing, the design presented here, is representative to a fully ceramic structure, which presents a flight relevant leading edge.

High temperature ceramic matrix composites (CMC), in particular carbon fiber reinforced silicon carbide (C/C-SiC) is highly suitable as thermal protection material [12]. At the DLR Institute of Structures and Design, C/C-SiC manufacturing is based on Liquid Silicon Infiltration (LSI), an economic and robust process which has been developed at DLR since the late 1980's [13]. The material was successfully tested as TPS during multiple flight test programs [22, 20]. Since the LSI-C/C-SiC material is very dense, normally it cannot be used for transpiration cooling. Therefore it was necessary to develop an optimized C/C-SiC for transpiration applications (OCTRA) [4].

The use of the permeable C/C-SiC also has the advantage that the single parts are in-situ joint during the siliconization providing higher mechanical properties of the final component. Contrary to the dense and impermeable C/C-SiC, OCTRA is characterized by selective insertion of cavities into the ma-

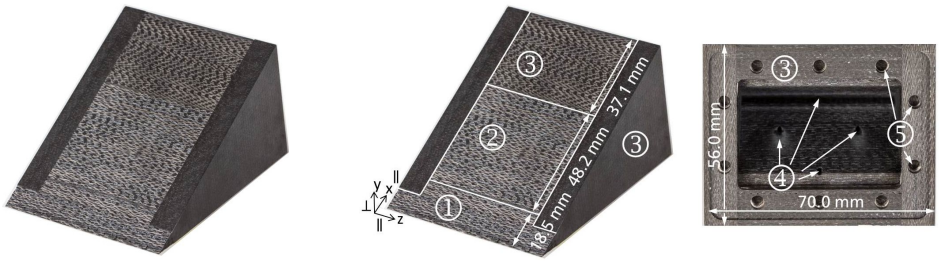

① OCTRA 40 ② OCTRA 20 ③ dense C/C-SiC
④ thermocouple holes ⑤ interface to sample holder

Fig 3. C/C-SiC wedge

Table 2. Material properties of OCTRA and classic C/C-SiC materials [4]

	k_D [10^{-13} m^2]	k_F [10^{-9} m]	$\lambda_{\parallel}$ [W/mK]	$\lambda_{\perp}$ [W/mK]	c_p [J/kgK]	ρ [kg/m^3]	e' [%]
OCTRA 40	7.5±1.02	19±0.83	15.9–18.0	8.37–12.5	607–1020	2060	9.08
OCTRA 20	1.68±0.18	4.05±0.18	16.4–20.5	8.0–11.71	604–907	2010	7.44
C/C-SiC	–	–	17.0–22.6	7.5–10.3	690–1550	2300	-

terial, by replacing fibers by non-stable fiber materials before pyrolysis. It is thus possible to adapt the flow characteristics inside OCTRA by means of porosity in a range of 1% up to 30% and thus also the permeability [5].

For the present study, a set of permeable material OCTRA 40 and OCTRA 20 was chosen, in order to provide the necessary cooling mass flow to the tip. The measured permeability for the OCTRA materials are shown in Tab. 2. The Darcy coefficient k_D for OCTRA 40 is approximately 4 times as high as that for the less permeable OCTRA 20 material. In addition, Tab. 2 also provides the thermal properties of the materials. It can be seen that the thermal conductivity varies strongly depending on the fiber direction but the variation over the materials in contrast is very low. The density for a all materials is measured with 2.0± 0.1 g/cm^3. Figure 3 shows the ceramic wedge with its basic dimensions and the material selection. The opening angle of the wedge was set to 31.15°, this angle corresponds to the planned opening angle of the SHEFEX III vehicle tip [3]. All other dimensions were selected, such that the entire wedge remains within the plasma jet even at different angles of attack.

The wedge itself is divided into three main parts, the tip (1) made of OCTRA 40, a center area (2) made of OCTRA 20 and dense C/C-SiC rear and side panels (3). Since the highest heat load will occur at the tip, this section needs to be cooled the most. In addition to permeability, the outflow behavior can also adapted by the geometry of the part. However, since the external geometry is usually given, the adjustment must be made on the internal side. On the CT-scan, shown in Fig. 6, the internal shape of the wedge is clearly visible. In addition to the inner geometry also the 4 type-K thermocouples positions are visible. The exact location of the thermocouples is given in Tab. 3 with respect to the coordinate system shown in Fig. 3. The inner opening angle is 22.0°, hence, the wall thickness is slightly increasing towards the rear. Along with the 2.5 mm thick and 7.5 mm deep notch at the tip and the permeability of the materials it is ensured, that the cooling gas is flowing in the direction of the highest heat load.

In order to attach the wedge to the sample holder, additional infrastructure is needed. In particular, gas supply in connection with the instrumentation of the thermocouples was challenging. Fig. 4 shows the interface parts used to connect the wedge into the plasma wind tunnel. The complete sample holder consists of three brass parts. The backplate of the wedge, labeled as (b), seals the reservoir of the wedge against the ambiance and connects the wedge to the sample holder. The remaining parts (c) and (f) are necessary in order to align the wedge in the direction of the plasma torch, with the possibility to adjust different angles of attack. The brass sample holder is water cooled with the in- and outlet lines marked with (e) in Fig. 4. In addition to the water cooling line, the gas supply for the

Table 3. Thermocouple locations on the wedge, Fig. 3

[mm]	TC-1 tip	TC-2 center(1)	TC-3 center(2)	TC-4 rear	SL-1 tip	SL-2 center	SL-3 rear
x	8.0	30.0	30.0	55.5	8.0	30.0	55.5
y	0.0	6.5	6.5	13.5	2.23	8.36	15.33
z	35.0	22.5	47.5	35.0	35.0	35.0	35.0

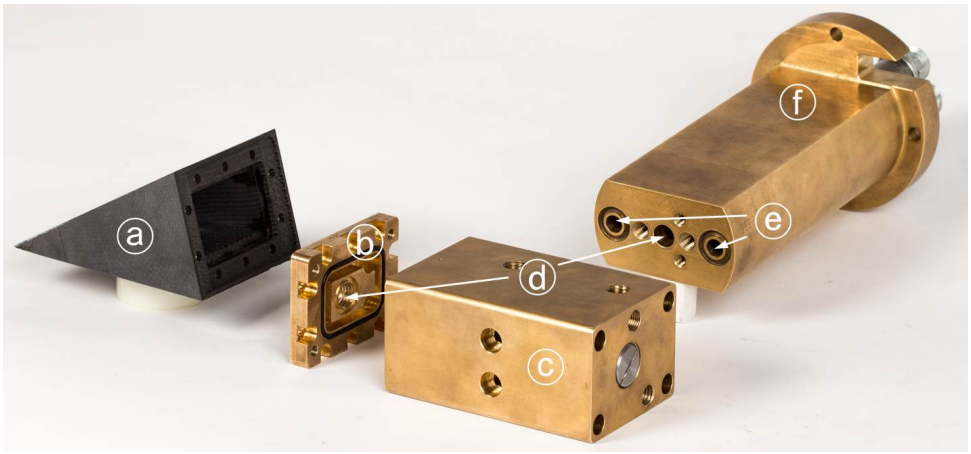

ⓐ wedge, see Fig. 3 ⓑ wedge sealing plate ⓒ sample holder adapter
ⓓ cooling gas supply ⓔ water cooling supply ⓕ sample base

Fig 4. Explosion view of the experimental setup

transpiration cooling ⓓ is included into the interface parts. Since the cooling gas has to be supplied all the way to the wedge, the instrumented thermocouples were routed into the wedge through the gas supply line.

In particular the ceramic C/C-SiC wedge is a unique, high temperature resistant part, which can be additionally cooled by transpiration cooling in order to expand the range of application even further.

5. Experiment Procedure

In order to show the effectiveness of transpiration cooling, the wedge was tested uncooled and at different cooling mass flow rates. The cooling mass flow rates used for the tests are given in Table 4.

As reference, a measurement without cooling was carried out at an angle of attack of 0° . The procedure foresees a parking position of the sample in the far off-axis aft of the plasma wind tunnel. In order to translate the sample into the plume, it is first moved in x-direction, parallel to the plume axis, towards the lid of the chamber and then translated into the plume in y-direction into the dedicated measurement location.

After establishing a pre-adjusted cooling mass flow rate, the wedge is translated into the plasma jet, as shown in Fig. 5. After a sufficient test period and the recording of the transient temperature data, the wedge is removed out of the plasma jet. After cooling down to its initial temperature, the next mass

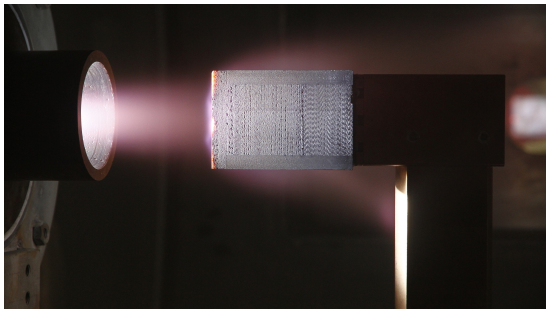

Fig 5. Wedge sample in plasma flow.

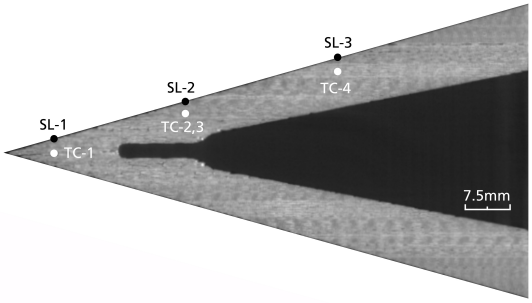

Fig 6. CT-scan of the internal wedge shape

Table 4. Tested cooling mass flows

$\dot{m}$ absolute $[g/s]$	0	0.85	2.55	4.25	5.95
$\dot{m}$ percentage [%]	0	10	30	50	70

flow rate is adjusted. During the cooling phase, it is ensured that all structural temperatures return to their stationary initial values.

In addition to the thermocouples, some measurements were accompanied by a thermal imaging camera (LumaSense MCS 640) to observe the surface temperatures. These measurements were used to determine the heat transfer and temperature distribution along the surface. The emissivity was set to 0.85 for all surface measurements. In order to compare certain positions on the surface with the thermocouples, three surface locations (SL) were defined. They are on the same x-position as the thermocouples but directly at the surface. The exact positions are defined in the Table 3.

In addition to the mass flow variations, the cooling efficiency of the wedge at different angles of attack to the flow was investigated. For this purpose, the wedge was first investigated at a symmetrical flow, i.e. angle of attack 0°, and later at an angle of attack of 12° respectively -12° to the flow. The 12° angle of attack leads to an oblique shock with a deflection angle of 27.57°. A smaller oblique shock occurs for an AoA of -12°, which corresponds to a deflection angle of 3.57°.

For a better presentation, the recorded temperature data have been smoothed by averaging the data with regards to a time step of 0.2 seconds. The two middle thermocouples (TC-2 and TC-3) are shown as average with their deviation from the average value.

6. Results

The transpiration-cooled wedge described in Sec. 4 was tested under the steady state flow condition at plasma wind tunnel PWK 4. Measurements as mentioned before, were taken by in-depth thermocouples at the tip, center and aft of the wedge along the wedge's axial centerline and 2D surface temperature measurement by an IR camera with an emissivity set to 0.85.

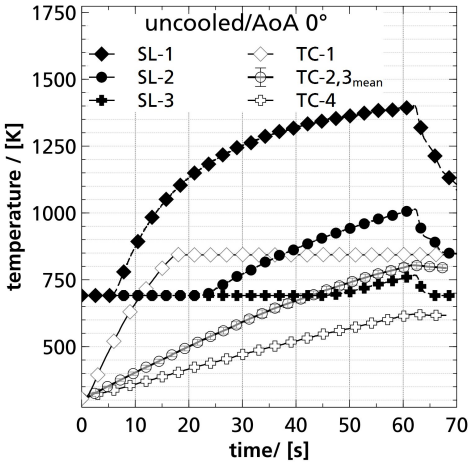

Fig 7. Temperature distributions over time at different locations without cooling and AoA 0°

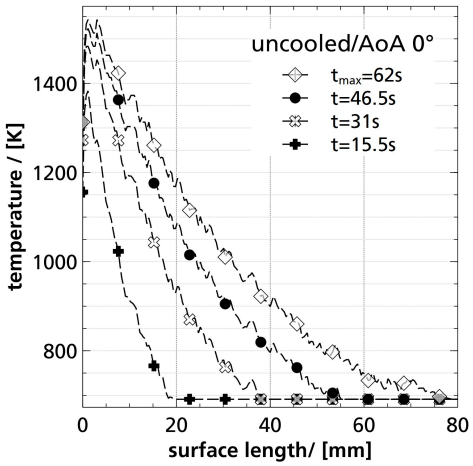

Fig 8. Temperature distributions without cooling and AoA 0° along the surface at different time points

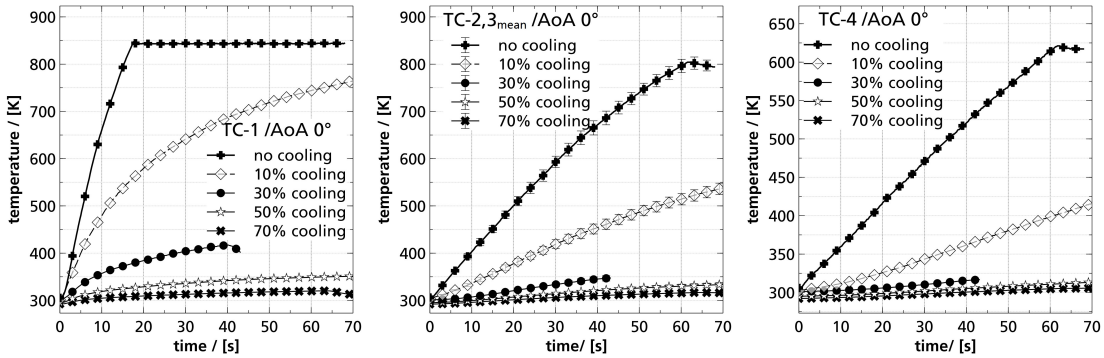

(a) Tip thermocouple **(b)** averaged mid-position TC **(c)** rear thermocouple

Fig 9. Temperatures for different cooling mass flows at different thermocouple locations, for AoA 0°

Thermal response of the wedge without cooling to the plasma flow is shown in Fig. 7 and 8. The measurements without cooling are used as a reference case to which the measurements under cooling are compared in order to evaluate the cooling efficiency. Figure 7 shows the data of the thermocouples over time, whereby the two middle thermocouples are shown as averaged. In addition, surface temperatures measured with the IR-camera are shown in the figure as well. The surface temperatures (SL) are taken along the central axis at the same x-position as the thermocouples with the y-value of the surface, as also indicated in Fig. 6. In particular, surface temperatures of up to 1500 K were measured at the tip. In Fig. 8, the surface temperature along the central axis is plotted for different time steps. The time t_{max} corresponds to the time of maximum heating. In this figure, it is particularly interesting how quickly the temperature drops along the surface. These temperature plots alone make it obvious that cooling is particularly important in the leading edge area, where temperatures rise dramatically towards the edge.

In the following, the results with cooling mass flow are now described and compared. In Figure 9a to 9c, the temperature curves recorded by the four thermocouples (see Tab. 3) are shown during the tests at an angle of attack of 0° for different cooling mass flow rates. Figure 9a, shows the temperatures from the thermocouple right at the tip. Especially for the uncooled case, a rapid temperature rise can be seen at the tip region. Within 18 seconds the temperature rises from about 293 K to over 880 K. Unfortunately, due to the settings of the data acquisition system it was not possible to follow the temperature signal further, so subsequently the line does not show a true temperature but rather a loss of the measuring signal. The maximum temperatures without cooling is already given in Fig. 7. Despite the relatively short measurement duration for the uncooled case, a significant temperature reduction can already be seen in comparison to the measurements conducted with cooling.

This trend can also be seen for the other thermocouple locations. However, for 50% and 70% cooling mass flow, the wedge seems to be overcooled, since the temperatures at the rear position, see Fig. 9c, do not exceed 315 K. The temperature offset at all positions between the two cooling mass flows is also very limited. Although the measurement with 30% cooling mass flow only had a measurement time of about 40 seconds, the measurement does not show any total overcooling of the wedge. At the tip the temperatures reached about 420 K after 40s. The fact that the cooling effect is still extremely high can be seen in comparison to the uncooled case. Considering the temperature distributions, the measurement with 10% cooling shows the best cooling characteristics. Although only a small amount of cooling mass flow is used (10% cooling), there is already a significant reduction in temperature. This is particularly noticeable for the two thermocouples in the middle, as shown in Fig 9b, where after 70 seconds the material is heated up to about 550 K. However, compared to the uncooled test the material

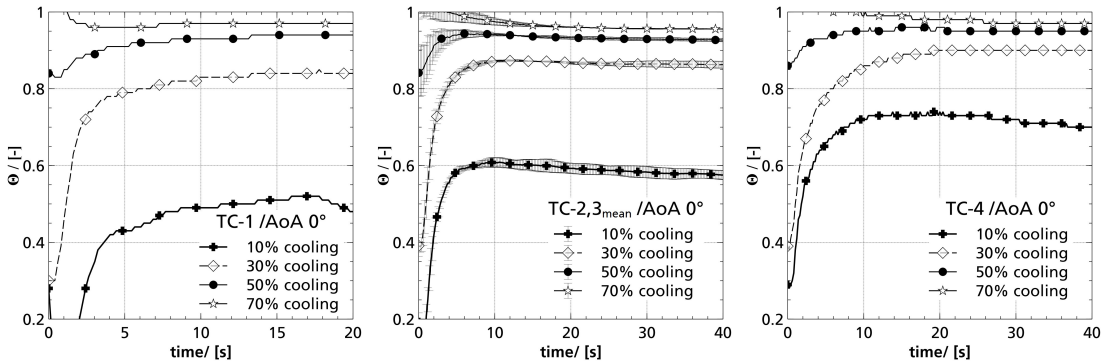

(a) Tip cooling efficiency **(b)** mid-position cooling efficiency **(c)** rear cooling efficiency

Fig 10. Cooling efficiency at different locations over time

could also be cooled down by about almost 270 K. The results show that a significant reduction of temperatures in the nose area can be achieved without overcooling the rear area. This is not to be expected within a structure without graded permeability.
However, in order to provide a better assessment of cooling efficiency, the results can be described by the dimensionless cooling efficiency

$$\theta = \frac{T_{uncooled,x} - T_{cooled,x}}{T_{uncooled,x} - T_{coolant}} \tag{2}$$

described by Langener et al. [15] for stationary temperature and from Böhrk [2] for transient systems. For the calculations based on equation (2), a constant coolant temperature of $T_{coolant} = 293$ K was chosen for all test cases. Figure 10 shows the calculated cooling efficiency for the tip, middle and rear area. For clarity reasons, the two middle thermocouples have been combined with their average value. The efficiency at the tip was evaluated up to 20 seconds, as the uncooled temperature data was available up to this point in time. The other cooling efficiency was calculated up to 40 seconds, in order to obtain a comparability with the cooling mass flow of 30%. The cooling efficiency applied over time basically confirm the conclusions drawn from the temperature data. It can also be seen here, that the entire component is overcooled with 50% or 70% cooling mass flow. Furthermore, for 30% and 10% cooling mass flow, the cooling efficiency increases from the tip to the rear. It is surprising that, contrary to the temperature curves, the cooling efficiency already approaches against a stationary value after a very short time from about 5-10 seconds. This is primarily due to the fact that the temperature rise is much faster during the uncooled test than for the cooled tests and therefore the denominator in equation (2) is increasing rapidly.

However, if the stationary cooling efficiency is plotted over the cooling mass flow, a good overview of the cooling efficiency can be achieved, as shown in Fig. 11. This overview shows, that for small mass flows the efficiency along the wedge increases, but the differences become smaller as the mass flow increases itself. The overall efficiency approaches the maximum of 1 for a maximum in cooling mass flow without any difference in the location. In terms of the efficiency the maximum of 1 means that the wall temperatures are reaching the same temperature as the coolant. However, from the figure a optimum can be derived, since in the beginning with small mass flows the increase in efficiency is a lot higher than in the region with high mass flows.

Since the cooling efficiencies, especially for 10% cooling mass flow, strongly depend on the position on the wedge, the question arises how well the permeability was adapted along the wedge. Figure 11 shows that for 10% cooling mass flow the cooling efficiency for the tip is around 0.5, but the rear area already reaches a value of 0.69. This gives the impression that the tip is considerably less cooled than

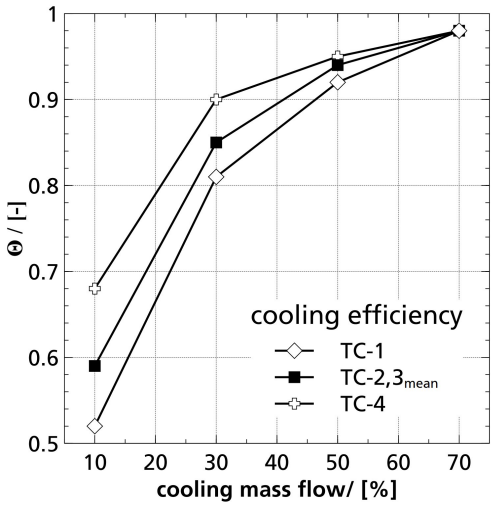

Fig 11. Stationary cooling efficiency over cooling mass flow

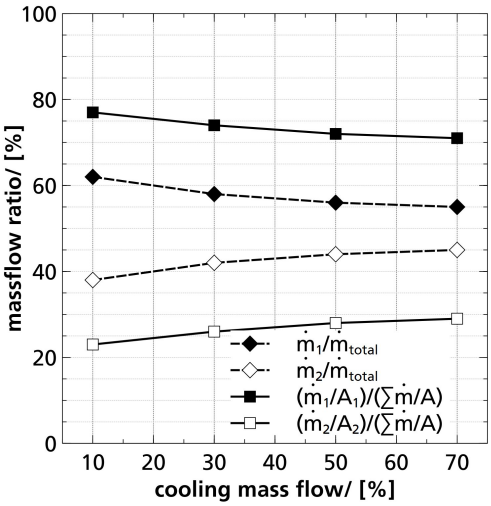

Fig 12. Mass flow and area specific mass flow distributions over total cooling mass flow

the rear area. Thus, in Fig. 12, the possible distribution of the mass flows as well as the area-specific mass flows (areas defined in Fig. 3 as (1) and (2)) are shown. Since only total mass flow and pressure difference was measured, the mass flow distribution shown in Fig. 12 are only estimations. It was assumed that along the wedge Δp over wall thickness is constant. Furthermore, the coolant temperature was assumed constant with a value of $T_{coolant} = 293$ K. With the assumptions made, an estimation of the cooling mass flow distribution can be made. As shown in Fig. 12, by grading the wedge, up to 60% of the cooling mass flow is passed through the area of the tip and only 40% through the less permeable area. If the area-specific mass flow rate is taken into account, it is even 80%. This means that in any case a gradation of permeability has taken place. The fact that a smaller cooling efficiency is still calculated for the tip area can probably be explained by the influence of temperature and the associated viscosity on the flow passing the wall. If the wedge had been built with a constant permeable material, it can be assumed that the differences in efficiency would be significantly higher between the areas.

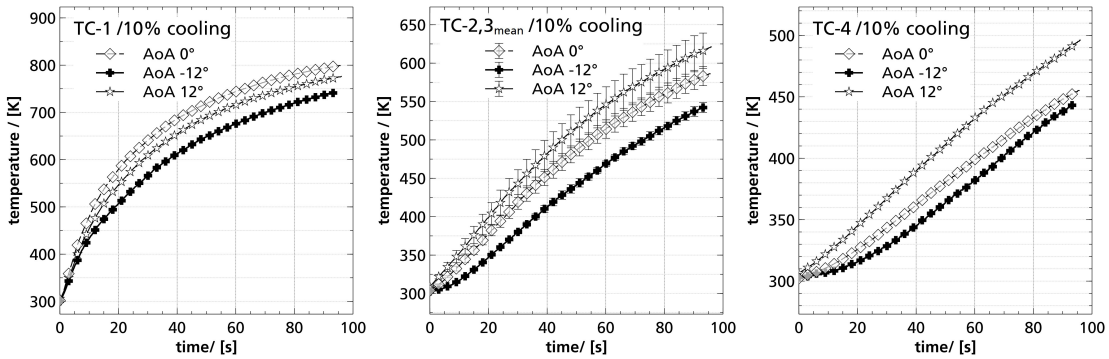

(a) Tip thermocouple **(b)** averaged mid-position TC **(c)** rear thermocouple

Fig 13. Temperature distribution for different AoA with 10% cooling mass flow.

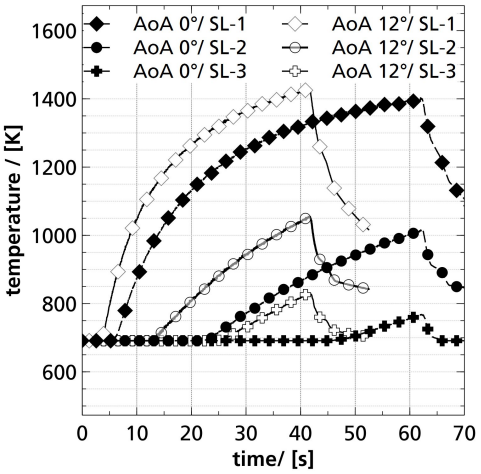

Fig 14. Unccoled surface temperatures over time at different AoA

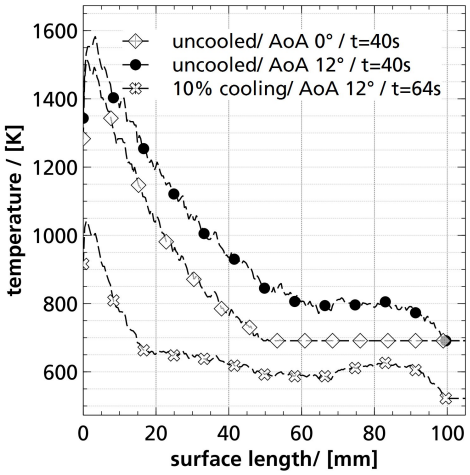

Fig 15. Surface temperatures over length for different AoA

In addition to the numerous measurements with symmetric flow, i.e. angle of attack 0°, measurements with the wedge, were also taken at different angles of attack. The wedge was tested with an angle of attack of 12°, forming a strong oblique shock on one side and smaller one the other. Since only one side of the wedge was instrumented with thermocouples, the wedge had to be measured once at 12° and once at -12° in order to characterize both flow patterns. However, in Fig. 13 the temperature distribution for different angles of attack is presented for a cooling mass flow of 10%. While the influence of the angle of attack on the temperatures can be clearly seen in the middle and rear area of the wedge, smaller deviations can be observed at the tip. Although the temperatures at the tip are more or less the same, the highest temperature can be found at an angel of attack of 0°, followed by 12° and -12°. Since the tip thermocouple is located on the symmetry axis, it is assumed that the temperatures measured at 12° and -12° are the same, as the thermocouple is heated up from both sides. However, these small derivations can be explained by heat conduction influence or an incorrect positioning of the thermocouple. At the other positions the temperature distribution is as expected.

Due to the strong oblique shock with a deflection angle of 27.57° (AoA 12°), the pressure and temperature is increasing which means less coolant is flowing in this direction. In contrast to this is the smaller shock with a deflection angle of 3.57° (AoA -12°), in which the pressure and temperature drops compared to the strong shock or the symmetrical flow, as a result more coolant is flowing in this direction. The influence of the oblique shock on the temperature distribution can also be seen at the surface, as shown in Fig. 14. In this figure the surface temperature at the defined surface location for the symmetric flow case (AoA 0°) and for the oblique shock (AoA 12°) over time is plotted. From the figure it is interesting to see that the temperature rises earlier in the case of an oblique shock than in the case of a symmetrical flow and will therefore probably also reach higher stationary temperatures. Figure 15 additionally shows both uncooled surface temperatures along the surface after 40 seconds. Moreover, it can be seen from the figure that the shock side not only has higher temperatures, but also a stronger temperature distribution to the rear.

Figure 15 also provides the surface temperature distribution for the 10% cooling case at an AoA of 12° after 64 seconds. Unfortunately, for the 10% cooling case surface data was only acquired starting from 64 seconds. Nevertheless, the temperature distributions can still be compared to the uncooled case. The temperature reduction compared to the uncooled AoA 12° case is immense, with a reduction at the tip region of 500K and 300K in the rear region, taken into account that the more comparable uncooled temperature at 64 seconds would be even higher. Particularly, the temperature distribution for the 10% case is notable. Contrary to the uncooled case, where the temperature drops to the rear, an

almost constant temperature could be achieved for the cooled case, especially between 18mm-90mm. This means that in this area the permeability and geometry were almost perfectly adapted to the cooling. Although the cooling effect at the tip is already tremendous, the permeability in this area would have to be increased or the permeability in the rear has to be decreased in order to get a constant temperature distribution along the wedge surface. However, compared to classic porous materials such as C/C, the effect of graded permeability is already visible with the presented wedge geometry and could be easily improved by further adjustments.

7. Summary

This paper presents the first results of a transpiration cooled wedge with an adapted permeability tested in high enthalpy flow. The wedge geometry is inspired by a sharp leading edge design and is manufactured entirely of fiber-reinforced ceramic material. This is the first time that it has been succeeded in manufacturing a structural component from various permeable materials for a high temperature application.
Equipped with thermocouples and a thermal imaging camera for surface measurement, the wedge was tested in the plasma wind tunnel PWK4 at the IRS of the University of Stuttgart in high enthalpy air flow. In order to achieve different flow conditions between the both wedge sides, the wedge was tested at different angles of attack $\pm$12°and AoA 0°for a symmetric flow condition. In parallel, different cooling mass flows were tested and compared to the case without cooling. As a global result, it can be deduced from the experiments that even with small mass cooling mass flows (0.85 g/s) a significant reduction of the material temperatures can be achieved. Expressed in numbers, the material temperature (cooling mass flow 0.85 g/s) for the thermocouple in the middle area of the wedge reached 450K after 40 seconds test time compared to almost 700K for the uncooled case. Furthermore, the results indicating that from a cooling mass flow of 3g/s the wedge is overcooled and the material temperatures practically do not rise. During the measurements of the surface temperatures it was noticeable that the temperatures along the surface strongly decrease without cooling. In the cooled cases, however, a homogeneous temperature could be achieved with the exception of the tip. This can directly be attributed due to the gradation of permeability along the wedge. The influence of the angle of attack and associated oblique shocks are more evident in the rear area of the wedge. The material temperatures measured on the shock side with the larger deflection angle were higher than on the other side or at the symmetric flow. This shows, in an unsymmetrical flow, the wedge must not only be adapted along the wedge but also between both sides of the flow.

Acknowledgment

The authors would like to thank the facility crew and workshops at DLR and at IRS for their support in making this cooperation a success. The support from Tobias Kuhn was helpful during the setup of the test campaign.

This work was supported by the Helmholtz Alliance as the Helmholtz Young Investigators Group VH-NG-909 *High Temperature Management in Hypersonic Flight*.

References

[1] M. Auweter-Kurtz, H. L. Kurtz, and S. Laure. Plasma generators for re-entry simulation. *Journal of Propulsion and Power*, 12(6):1053–1061, Nov 1996.

[2] H. Böhrk. Transpiration-Cooled Hypersonic Flight Experiment: Setup, Flight Measurement, and Reconstruction. *Journal of Spacecraft and Rockets*, 52(3):674–683, Apr 2015.

[3] C. Dittert, H. Böhrk, and H. Elsässer. Design of a Transpiration Cooled Sharp Leading Edge for SHEFEX III. In *8th European Conference on Aerothermodynamics for Space Vehicles*, March 2015.

[4] C. Dittert and M. Kütemeyer. Octra - Optimized Ceramic for Hypersonic Application with Transpiration Cooling. In *Advances in High Temperature Ceramic Matrix Composites and Materials for Sustainable Development*, volume 263 of *Ceramic Transactions*, chapter 37, pages 389–399. Wiley-Blackwell, 2017.

[5] C. Dittert, M. Kütemeyer, M. Kuhn, and A. Wagner. Process Optimization of Ceramic Matrix Composites for Ultrasonically Absorptive TPS Material. In *2018 Joint Thermophysics and Heat Transfer Conference*, AIAA AVIATION Forum. AIAA, Jun 2018.

[6] C. Dittert, M. Selzer, and H. Böhrk. Flowfield and Pressure Decay Analysis of Porous Cones. *AIAA Journal*, 55(3):874–882, Jan 2017.

[7] E. Eckert and J. Livingood. *Comparison of Effectiveness of Convection-, Transpiration-, and Film-cooling Methods with Air as Coolant*. NACA technical report. National Advisory Committee for Aeronautics, 1954.

[8] D. Glass. Ceramic Matrix Composite (CMC) Thermal Protection Systems (TPS) and Hot Structures for Hypersonic Vehicles. In *15th International Space Planes and Hypersonic Systems and Technologies Conference*. AIAA, Apr 2008.

[9] D. Greuel. *Untersuchungen zum Impuls- und Stofftransport in effusiv gekühlten faserkeramischen Raketenbrennkammern*. PhD thesis, RWTH Aachen, 2012.

[10] S. Gulli and L. Maddalena. Characterization of Complex Porous Structures for Reusable Thermal Protection Systems: Effective-Permeability Measurements. *Journal of Spacecraft and Rockets*, 51(6):1943–1953, Sep 2014.

[11] H. Hald. *Faserkeramiken für heiße Strukturen von Wiedereintrittsfahrzeugen - Simulation, Test und Vergleich mit experimentellen Flugdaten*. PhD thesis, Universität Stuttgart, 2001.

[12] H. Hald, H. Weihs, T. Reimer, and T. Ullmann. Development of Hot CMC Structures for Space Reentry Vehicles via Flight Experiments. In *International Air and Space Symposium (Evolution of Flight)*. AIAA, Jul 2003. 0.

[13] B. Heidenreich. C/SiC and C/C-SiC Composites. In *Ceramic Matrix Composites: Materials, Modeling and Technology*, chapter 6, pages 147–216. Wiley-Blackwell, 2014.

[14] M. Kuhn and H. Hald. Application of Transpiration Cooling for Hot Structures. In *RESPACE - Key Technologies for Reusable Space Systems*, pages 82–103. Springer Berlin Heidelberg, 2008.

[15] T. Langener, J. von Wolfersdorf, M. Selzer, and H. Hald. Experimental investigations of transpiration cooling applied to C/C material. *International Journal of Thermal Sciences*, 54:70–81, 2012.

[16] M. J. Lewis. Sharp Leading Edge Hypersonic Vehicles in the Air and Beyond. SAE International, 1999. 1999-01-5514 ER.

[17] S. Loehle, S. Fasoulas, G. Herdrich, T. Hermann, B. Massuti-Ballester, A. Meindl, A. S. Pagan, and F. Zander. The Plasma Wind Tunnels at the Institute of Space Systems: Current Status and Challenges. In *32nd AIAA Aerodynamic Measurement Technology and Ground Testing Conference,*. AIAA, 2016.

[18] J. M. Longo, J. Turner, and H. Weihs. SHEFEX II - Aerodynamic Re-Entry Controlled Sharp Edge Flight Experiment. In *6th European Symposium on Aerothermodynamics for Space Vehicles*, November 2008.

[19] D. Prokein, C. Dittert, H. Böhrk, and J. von Wolfersdorf. Transpiration Cooling Experiments on a CMC Wall Segment in a Supersonic Hot Gas Channel. In *2018 International Energy Conversion Engineering Conference*, AIAA Propulsion and Energy Forum. AIAA, Jul 2018. 0.

[20] T. Reimer. The KERAMIK Thermal Protection System Experiment on the FOTON-M2 Mission. In *5th European Workshop on Thermal Protection Systems and Hot Structures*. ESA, May 2006.

[21] R. Viskanta, X. Fu, and J. P. Gore. Measurement and correlation of volumetric heat transfer coefficients of cellular ceramics. *Experimental Thermal and Fluid Science*, 17(4):285–293, 1998.

[22] H. Weihs. Sounding Rockets for Entry Research: SHEFEX Flight Test Program. In L. Ouwehand, editor, *21st ESA Symposium on European Rocket and Balloon Programmes and related Research*, volume SP-721, pages 143–152. ESA, October 2013.

[23] Y. Zhu, S. Ohtani, Y. Sato, and N. Iwamoto. The improvement in oxidation resistance of CVD-SiC coated C/C composites by silicon infiltration pretreatment. *Carbon*, 36(7):929–935, 1998.